# Residual stress characterization of single and triple-pass autogenously welded stainless steel pipes

**R.D. Haigh, M.T. Hutchings, M.E. Fitzpatrick, J.A. James, S. Okido, R. Mizuno, K. Ogawa, D.J. Hughes.**

## Abstract

Using neutron diffraction the components of the residual stress field have been determined in the region near a mid-length groove in two identical austenitic stainless pipes in which weld beads had been laid down. One pipe sample had a single pass, and the second a triple pass, autogenous weld deposited around the groove circumference. The results show the effect on the stress field of the additional weld deposited and are compared to the results of Finite Element Modelling. The hoop stress component is found to be generally tensile, and greater in the triple pass weldment than in the single pass weldment. The hoop stresses reach peak values of around 400 MPa in tension. X-ray measurements of the residual stress components on the near inner surface of the pipe weldments are also presented, and show tensile stresses in both pipes, with a higher magnitude in the three-pass weldment.

## 1. Introduction

The primary area of component cracking in power plant piping is in welded joints. One of the main causes of failure in welded pipes is stress corrosion cracking (SCC), and the likelihood of this occurring is highly-dependent on residual stresses present in the weld region. Prediction of the magnitude and profile of the residual stress distribution in coolant pipe work is extremely difficult, and experimental validation of finite element-based models of residual stress generation is required [1], [2], [3] and [4]. The work described here is part of a programme aimed at understanding the residual stress built up in circumferential weldments in austenitic steel pipes.

Neutron diffraction techniques are a powerful means for non-destructive in-depth determination of residual stresses [5]. By fabrication of plant-scale mock-ups using controlled fabrication conditions, experimental samples can be provided in which the fabrication history is well-defined. Measurement of such samples can provide knowledge of the residual stresses arising from thermal histories during welding. During the cool down and solidification following a weld pass deposition, molten material will shrink and tend to pull all other material with it. In the case of butt-welded pipe weldments this manifests itself as a circumferential contraction about the girth weld. The parent metal near to the heat-affected zone (HAZ) will partially resist the deformation, and it is this partial resistance or partial flow which results in residual stresses. After welding, tensile residual stresses usually develop in both the weld metal and the heat-affected zone (HAZ) metal. The magnitude of the residual stress field is affected by the pipe's diameter, its thickness, and the size of the weld bead. Girth weld beads generally lead to high tensile residual stresses on the inside surface of the pipe [1]. In particular it is tensile residual stresses in the HAZ which contribute to SCC. Successive weld passes, in a multi-weld pass weld, will result in a cyclic accumulation of both residual elastic stresses and plastic strains.

This work is aimed at determining how stresses develop as the number of weld passes increases. By comparison with predictions from Finite Element Modelling (FEM) the neutron diffraction results will help validate FEM analysis of the change in stress profile in welded pipes on filling the weld. The results of near-inner surface measurements using X-ray diffraction are also presented.

There has been much work done in the last two decades on comparison between measured and modeled residual stresses in welded components [10] and [11]. This has led to improvements in both experimental and modelling approaches to the determination of weld residual stress. However,

the geometries studied have generally been relatively simple, such as a bead-on-plate or bead-in-groove specimen [12]. In this study, we have looked at a more complex geometry, with the intention of understanding the residual stress generation in autogenous welds. The modelling is used to provide support to the experimental data. This complements the wider body of work on the determination of residual stress in materials and components for nuclear power and similar applications [13], [14], [15], [16], [17], [18], [19] and [20].

In complementary work related to that presented here, neutron diffraction has been used to measure the residual stress distribution throughout the weld area in two specially fabricated multi-pass girth-welded austenitic stainless steel pipes of similar dimensions to those discussed here. However in that case the weldments were formed by joining two half-length sections of pipe, where one weldment had weld metal deposited in the joining groove up to half the pipe wall thickness, and one with weld metal deposited up to full pipe wall thickness [6].

## 2. Sample weldments

### 2.1. Manufacture

The two samples examined were fabricated from a length of austenitic stainless steel pipe, type 304. The starting material was a 3500 mm length of pipe of outer diameter 318.5 mm and inner diameter 251.9 mm. This was cut and ground to make two pipes of length 500 mm with outer diameter 305 mm and inner diameter 255 mm. These sample pipes were then subjected to solution annealing in vacuum, with a heating rate of <200 °C per hour, a hold temperature of 900 °C ± 5 °C for 2 h, followed by cooling at a rate of <275 °C per hour.

A groove was then cut to a depth of half the wall thickness around the mid-length diameter, with dimensions shown in Fig. 1. Weld beads were then laid down in the flat position inside the groove by automatic TIG welding (GTAW). The welding current was 132 A, voltage 10 V, and speed 9 cm/min. There was no pre-heating. The inter-pass temperature was <150 °C. The composition of the parent pipe metal and the weld metal is given in Table 1.

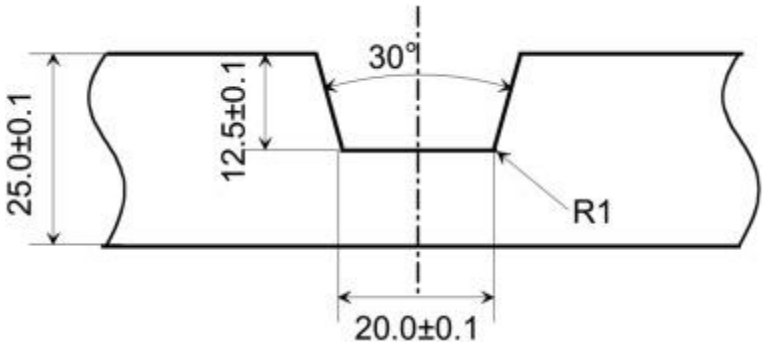


Fig. 1.

The dimensions in mm of the groove cut at the mid axis point of the pipes.

Table 1.

The chemical composition of the austenitic stainless steel pipe, type 304.

| | Composition/wt % | | | | | | | |
|---|---|---|---|---|---|---|---|---|
| | **C** | **Si** | **Mn** | **P** | **S** | **Ni** | **Cr** | **Fe** |
| Pipe (Parent) Metal | 0.010 | 0.42 | 1.49 | 0.019 | n.d. | 9.15 | 18.19 | 70.72 |

**2.2. The co-ordinate system**

It was necessary to carefully establish a sample coordinate system for each weldment in order to define the measurement positions. This is shown in Fig. 2. Here x, y, z are Cartesian axes with origin at the centre of the weldment. The x axis is along the axial direction of the pipe, and the z axis along a radial direction defined by the azimuthal angle $\alpha = 0$. Measurement angles and radii were denoted as $\alpha$ and $r$ respectively as shown in Fig 2(iii). The azimuthal angles $\alpha$ were engraved on each weldment in steps of 90°. It should be noted that $\alpha$ is taken as positive in the clockwise direction when looking along the axial negative x direction, with zero angle along the +z axis. The shape of the pipe weldment lends itself to a cylindrical coordinate system, which is here expressed as $r$, $\alpha$, $x$. A reference point denoted **T**, top dead centre (TDC), was located in these cylindrical coordinates at (139.07, 0, 250), and in the Cartesian coordinates at (250, 0, 139.07), as shown in Fig. 2 and Fig. 3. An access slot aperture was machined at the 90° position with its centre at Cartesian coordinates (0, 140, 0) in order to facilitate access by the neutron beam through minimising absorption losses of beam intensity. It is assumed that this slot will not affect the stress distribution as it is distanced from the measurement positions.

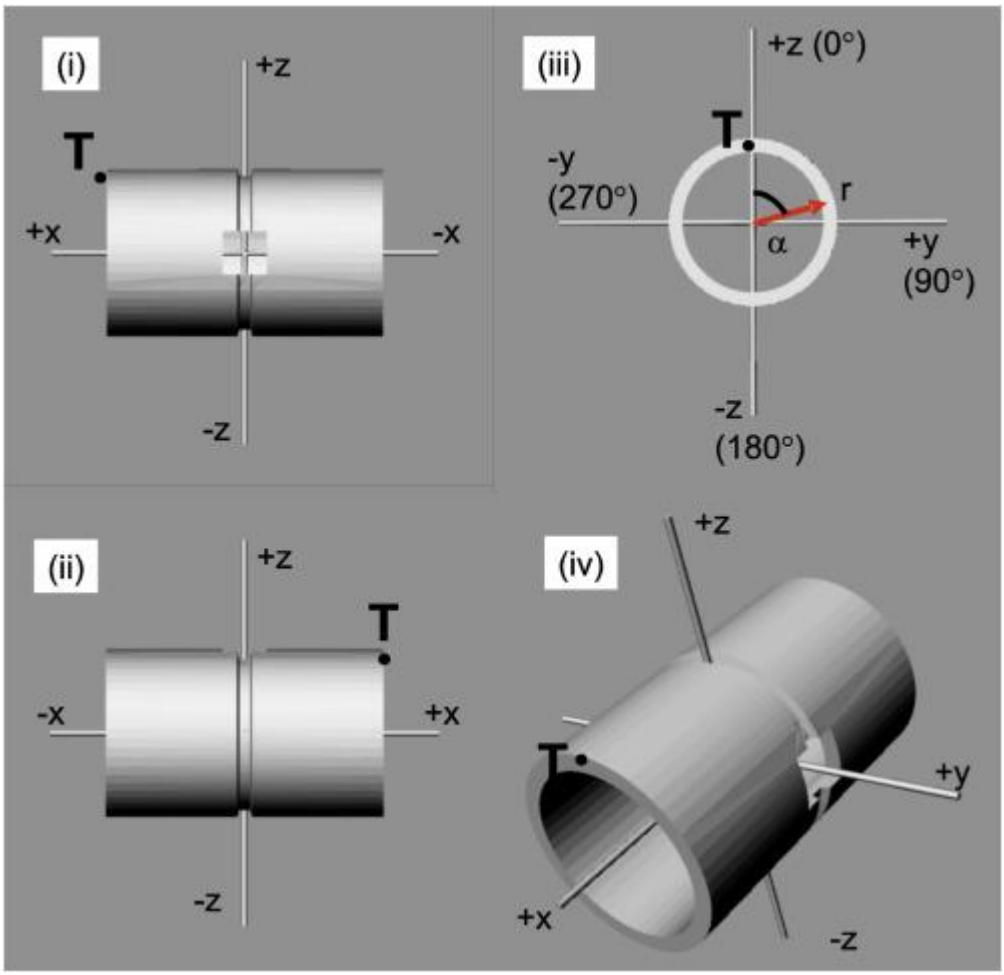


Fig. 2.

(i) Autogenous pipe weldment relative to Cartesian coordinate system (x,y,z) with origin at the centre of the pipe weldment. The view along negative y shows the position of the neutron access aperture. The reference point top dead centre (TDC) is marked with a capital T. (ii) The view along positive y, opposite to the neutron access aperture. (iii) Plan view of the pipe looking along negative x, with TDC and positive x axis pointing upwards out of the plane of the page. This view shows the radius r and azimuthal angle α. It should be noted that $\alpha$ is taken as positive clockwise when looking along the negative x direction as shown. (iv) Oblique view.

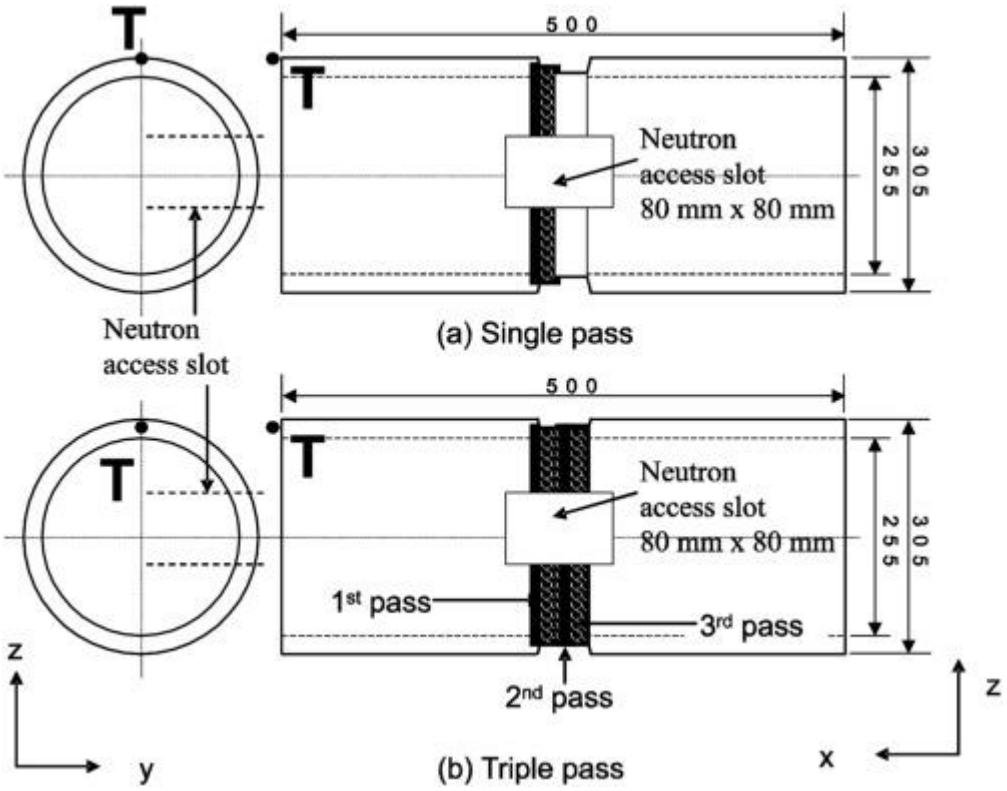


Fig. 3.

Showing the position of the welding passes with respect to the x,y,z axis. The single-pass and triple-pass weldments are shown in (a) and (b) respectively. Dimensions shown are in mm. The reference point top dead centre (TDC) is also shown with respect to the coordinate system, and has been marked with a capital T, the positive y axis points upwards out of the plane of the page. In the case of both plan views (left) the positive x axis points upwards out of the plane of the page.

Both pipes were circumferentially welded autogenously around the central groove. The weld was laid down in the increasing α direction, with the first and third pass start and stop positions being at the $\alpha$ = 0° position, and the second pass start and stop positions being at $\alpha$ = 180°. For each weld pass the moving heat source was briefly paused at the position 180° from start. The dimensions of the single-pass pipe weldment and the position of the weld pass with respect to the x axis are shown in Fig. 3a, the centre of the single pass weld is at x = +6.6 mm. The position of the three weld passes in the triple-pass weldment, which is of the same dimensions, and their order with respect to the x axis filling the groove, are shown in Fig. 3b, their centres are at x = +6.6 mm, 0 mm, and −6.6 mm.

**3. The neutron diffraction measurements**

The neutron diffraction method of residual stress measurement [5] is based on measurement of the lattice strain, averaged over a gauge volume in the sample. The difference in lattice spacing, *d*,

determined from the Bragg angle of diffraction from the gauge volume, relative to that, $d_0$, from a reference strain-free sample is used to calculate strain Σ as:

$\sum=(d-d_0)/d_0 \sum=(d-d0)/d0$

The measurements were made on the SALSA instrument at the Institute Laue Langevin, Grenoble [7]. This instrument is situated on a thermal guide which transports the neutrons from the reactor onto a bent silicon monochromator. The angle of the diffracted beam from the monochromator is defined by a soller slit collimator. This defines the wavelength of the incident beam on the sample, and the beam area is defined by a slit aperture. The diffracted beam from the sample is defined by a slit aperture close to the sample and a two-dimensional (2D) position-sensitive detector. This slit aperture and detector can be rotated about the sample table axis to define the angle, $2\vartheta$, of the diffracted beam relative to the incident beam. The two slit apertures can be adjusted in position relative to the sample along the incident and diffracted beam directions, and their size defines the size of the instrumental gauge volume, over which the average strain is measured. This gauge volume is centred at the intersection of the incident and diffracted beam paths, over the vertical rotational axis of the sample table.

The sample is mounted on the table of a hexapod, which is a device enabling the sample table to be moved in X, Y, Z, ω and ψ senses, where ω and ψ are the table rotation angle and the table tilt angle respectively. As the weldments were of cylindrical geometry the tilt option was not used in the measurements.

The direction of the component of strain measured is given by the direction of the scattering vector, **Q**, which bisects the incoming and diffracted neutron beam, relative to the weldment.

Since the two pipe samples were of the same dimensions and of true cylindrical form, mounting on the SALSA instrument was in fact quite straightforward.

The measurements were made in two stages, with the set-up of the instrument as similar as possible for each stage. The main difference in set-up was a slightly larger incident neutron wavelength of 1.740 Å used in the second stage compared with 1.695 Å used in the first stage. Powder samples of α-iron and γ-stainless steel were used for calibration and normalisation of the two stages of measurement. The {311} reflection from the stainless steel was used to measure the strains with a diffraction angle, $2\vartheta$, of about 102°. All measurements were made with the 2D detector fixed in angle, the small shifts in $2\vartheta$ being measured by shifts in peak intensity channel on the detector.

For the measurement of hoop and radial strain components each weldment was carefully positioned, using accurately aligned camera-image theodolites, on the sample table with its axis vertical and the centre of the weldment, x = y = z = 0, at the centre of the instrumental gauge volume. At this position the instrumental translations TX, TY, and TZ were set to zero. The weldment was then moved so that the measurement position was at the centre of the gauge volume using these three instrument translations. For measurement of the axial component, the weldments were mounted on a special table supplied by JNES in which the axis was horizontal on the instrument. The weldments could be rotated about this axis, and translated, to bring the desired position into the centre of the gauge volume.

One set of measurements was made at positions in the centre of the groove at x = 0 mm, around a circumferential arc at α = −25°, −20°, −15°, −10°, −5°, 5°, 15°, 20°, 25° and at 190° and 270°. Measurements at positions with α = −7°, 0°, 10°, and 180° were also made. These are termed here as

'arc' measurements. All arc measurements were made at three radii, $r$ = 130.5 mm, 134.5 mm and 137.5 mm. It should be noted that the depth below the bottom of the groove is equal to (140 − $r$) mm. A small gauge volume of 3 × 3 × 3 mm$^3$ was used for positions directly beneath the welds at $r$ = 137.5 mm, in both pipe weldments, giving higher spatial resolution in the weld region. Measurements made elsewhere, at $r$ = 134.5 and at $r$ = 130.5 mm, in both weldments were made with a 4 × 4 × 4 mm$^3$ gauge volume.

An additional set of measurements was made at positions along the axial x-axis at different azimuthal angles, shown in Fig. 4 with respect to the weld groove. These are termed 'map' measurements. To avoid partial filling of the gauge volume, the positions having gauge volumes of 3 × 3 × 3 mm$^3$ and 4 × 4 × 4 mm$^3$ were measured at 2.5 mm and 3 mm from the nearest surfaces respectively. The variation of strain was measured at positions along the x-axis at $r$ = 130.5, 134.5 and 137.5 mm, that is at distances of 3.0, 7.0, and 10.0 mm respectively from the inner surface of the pipe, and 9.5, 5.5 and 2.5 mm from the bottom of the groove. However for the positions at x = ±20 mm measurements were made at $r$ = 138.5 mm rather than 137.5 mm.

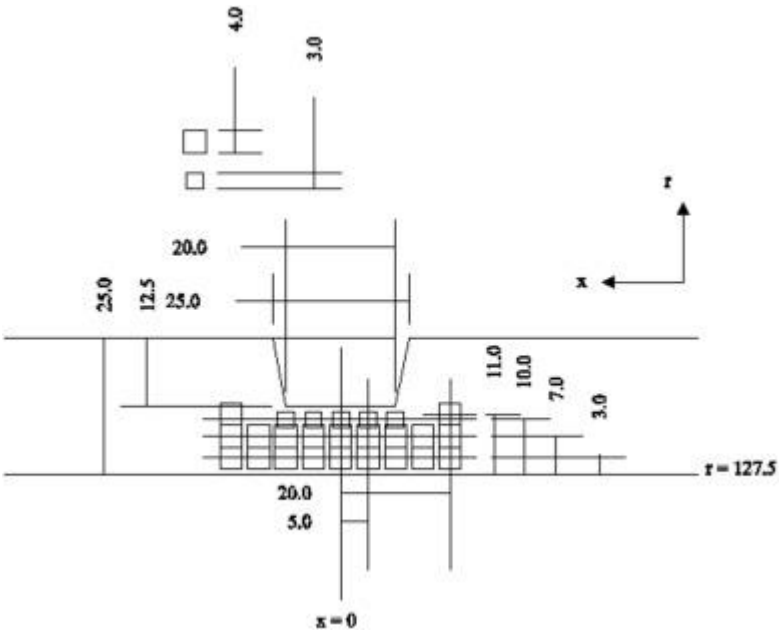


Fig. 4.

Position of the 'map' measurements (centre of the drawn squares) in relation to the weldment groove. All dimensions are in mm. The radial positions of all above positions through the pipe thickness are expressed relative to the inner pipe radius at r = 127.5 mm.

### 3.1. Stress-free reference and calibration

The reference stress-free values of $d_0$ from which strain values were calculated were obtained from measurements on 6 × 6 × 6 mm$^3$ cubes of parent metal or HAZ. These cubes were each made up from eight 3 × 3 × 3 mm$^3$ cubes carefully cut from the appropriate region of the section that had been removed from each weldment to form the beam slot opening. These eight small cubes were then stuck together maintaining the orientation relative to the weldment axes. Two 6 × 6 × 6 mm$^3$ cubes were formed from both parent metal and HAZ regions from each weldment, so that a check

on consistency of the data could be made. The composite cubes were carefully placed at the centre of the gauge volume for measurement of the {311} diffraction peak with the scattering vector **Q** in the axial, hoop and radial directions in turn. A gauge volume of 3 × 3 × 3 $mm^3$ was used to ensure that it was completely immersed in the cubes and that no edge effects were present.

Although the size of the 3 × 3 × 3 $mm^3$ reference cubes should ensure that the macrostress in these samples is relieved, there may be microstress present, in particular intergranular stress from any plastic deformation in the weldment. Since the aim of the measurements is to determine the macrostress in each weldment, by using reference samples from the corresponding location and direction to that being measured in the weldment, any microstress should cancel. *A priori* the intergranular stress could be anisotropic. However in both stages of measurement there was no clear evidence of anisotropy of strain in the reference samples, rather a random variation of $d_0$ was found which was rather larger than the expected uncertainty. The values of the stress-free reference $d_0$ used to determine each strain were therefore taken as the average of values for each of the axial, hoop and radial direction of **Q** in each reference cube material from each weldment, with uncertainties given by the standard deviation from the average. All the strain measurements are of shifts in {311} diffraction angle from the weldment with respect to the appropriate stress-free diffraction angle in each set of measurements to give ($d - d_0$). This difference in lattice spacing must be determined as accurately as possible from the shift in diffraction angle and is the principal contribution to the accuracy of strain measurement. The uncertainty in absolute value of $d_0$ itself contributes directly to the uncertainty in the strain measurement and so ∼1% accuracy is sufficient. In order to compare directly the data from the two stages of experiment, a few measurement points were repeated. Another check on consistency was to confirm a smooth variation of the results, especially of strain versus position, which included data from both experiments.

### 3.2. Calculation of residual stress

It is assumed throughout that the principal stress and strain directions are in the axial, radial and hoop direction of each weldment. From the {311} diffraction peak angles measured with scattering vector **Q** in these three directions, and the corresponding diffraction angles measured on the small cube samples, assumed to be macrostress-free, the three principal residual strain components were calculated. The three principal stress components were then calculated using values from Kröner modelling of the elastic constants [5] of 183.5 GPa for the Young's modulus for the 〈311〉 direction, and a value of Poisson's ratio $\upsilon$ = 0.31.

## 4. Results

### 4.1. Arc measurements

The results of the variation with azimuthal angle $\alpha$ of the three stress components at x = 0 are presented in Fig. 5, Fig. 6 and Fig. 7.

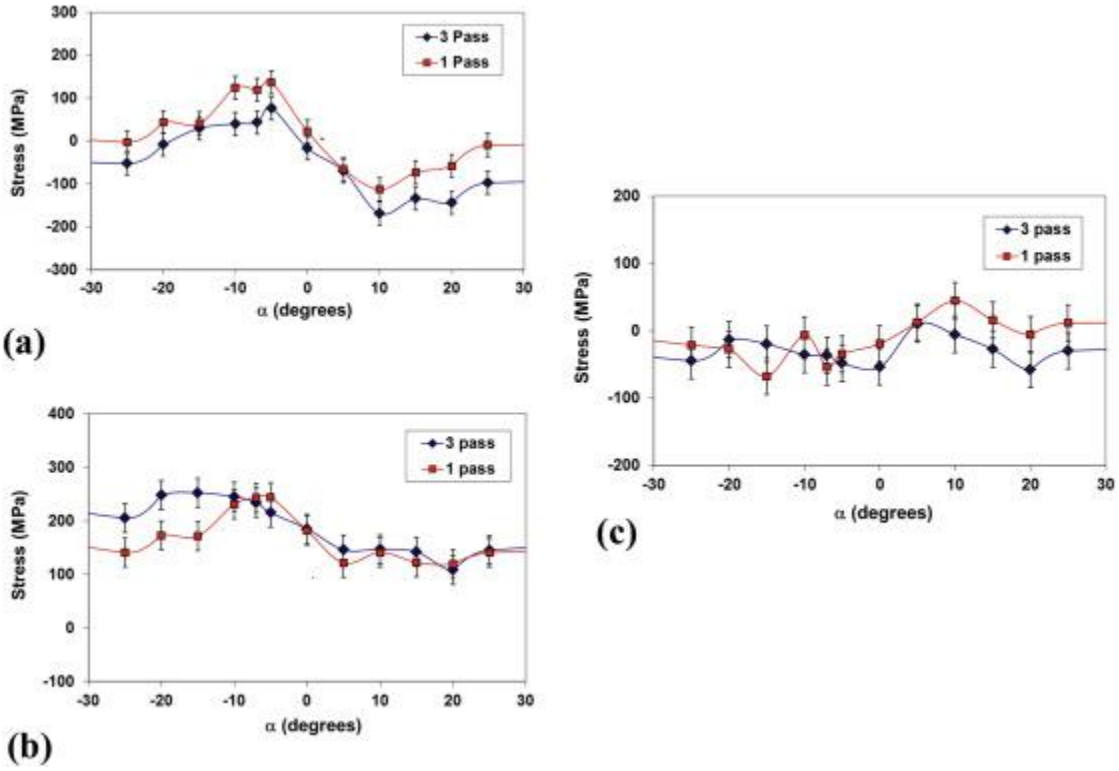


Fig. 5.

Comparison of the results of '*arc*' measurements on the single-pass and triple-pass weldments, at x = 0, r = 130.5 mm for (a) Axial (b) Hoop (c) Radial stress component.

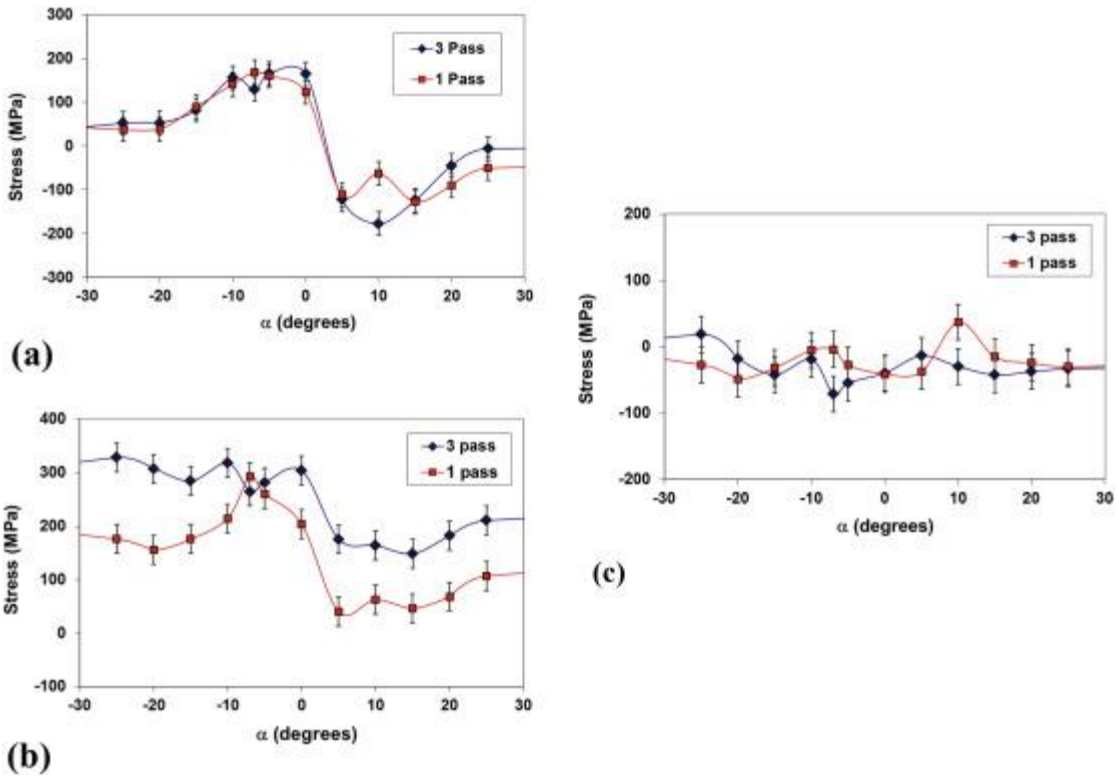


Fig. 6.

Comparison of the results of '*arc*' measurements on the single-pass and triple-pass weldments, at x = 0, r = 134.5 mm for (a) Axial (b) Hoop (c) Radial stress component.

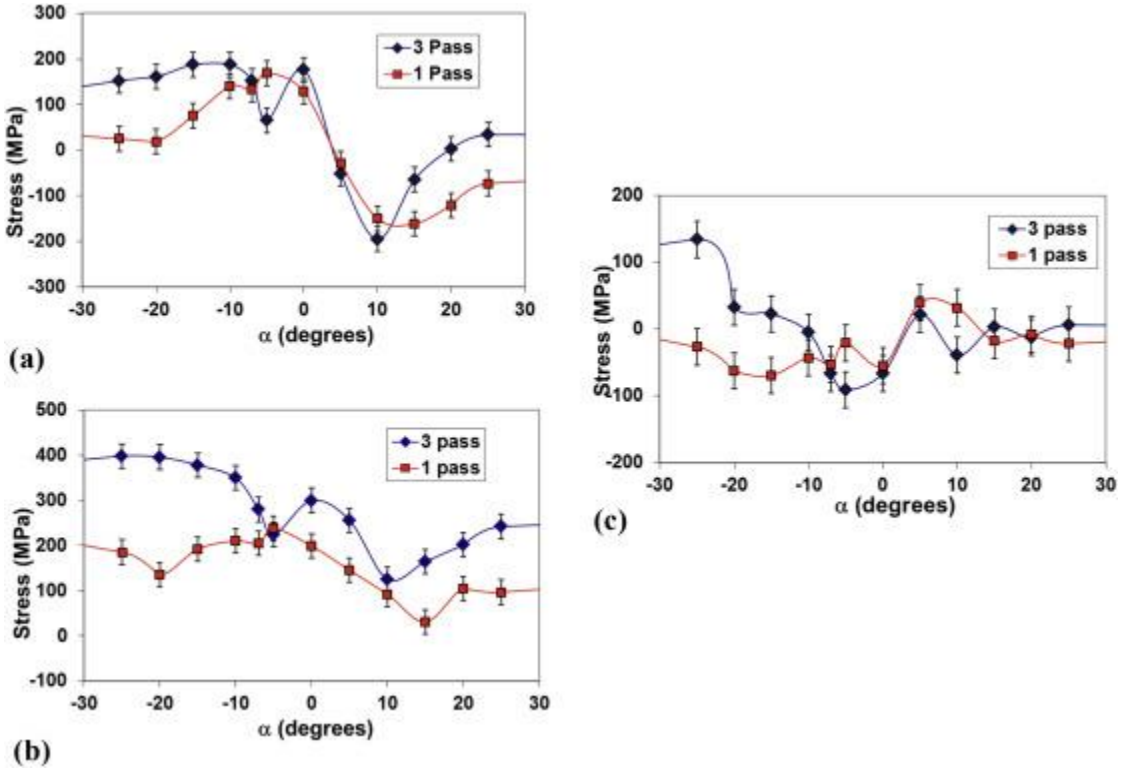


Fig. 7.

Comparison of the results of '*arc*' measurements on the single-pass and triple-pass weldments, at x = 0, r = 137.5 mm for (a) Axial (b) Hoop (c) Radial stress component.

Of particular interest in the axial stress component is the tensile to compressive transition through $\alpha = 0$, observed in both the single and triple-pass weldment on going from negative to positive $\alpha$. This variation increases as $r$ increases. All hoop stress components are tensile; however they become less tensile on going from negative to positive $\alpha$. This tensile stress is higher in the case of the triple-pass sample.

Measurements near $\alpha = 180°$ showed a reduction in tensile stress in the single-pass weldment between 180° to 190° in both the axial and hoop components, suggesting an effect caused by pausing the welding heat source in this case. This effect is much less in the triple-pass weldment.

The radial stress component is close to zero for both weldments, except for a tensile stress at the largest radius and most negative $\alpha$ in the triple-pass weldment.

**4.2. Map measurements**

The results of the measurements of the three residual stress components variation along the axis at $\alpha = 0$ are shown in Fig. 8, Fig. 9 and Fig. 10. In all cases the position of the single weld pass, and the first weld pass in the triple-pass weldment is at the left hand side of the graphs, in the region of x = +6.6 mm.

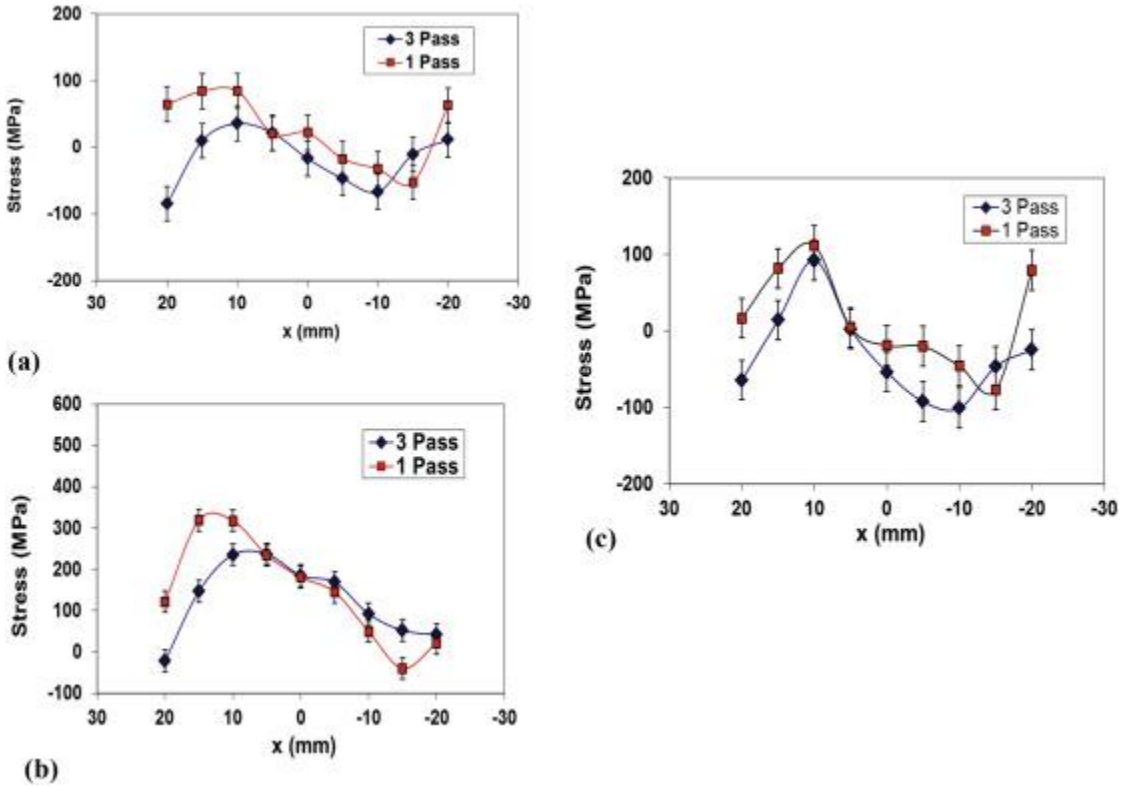


Fig. 8.

Comparison of the results of '*map*' measurements on the single-pass and triple-pass weldments, at α = 0, r = 130.5 mm for (a) Axial (b) Hoop (c) Radial stress component.

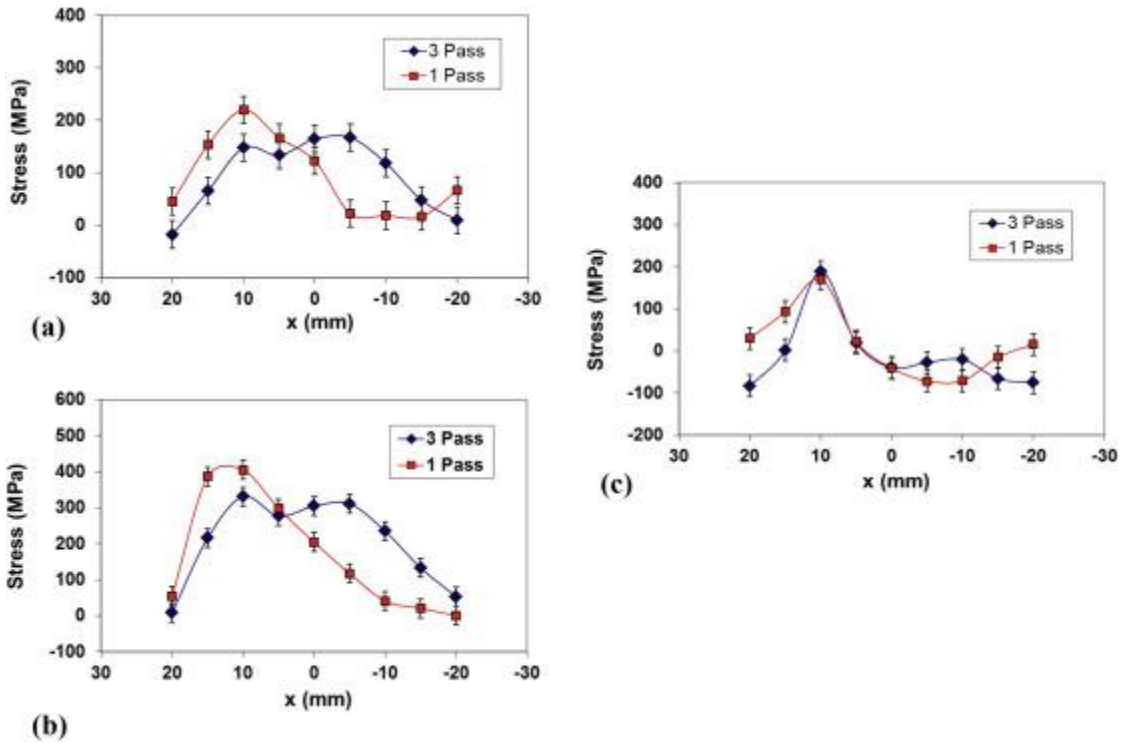


Fig. 9.

Comparison of the results of '*map*' measurements on the single-pass and triple-pass weldments, at α = 0, r = 134.5 mm for (a) Axial (b) Hoop (c) Radial stress component.

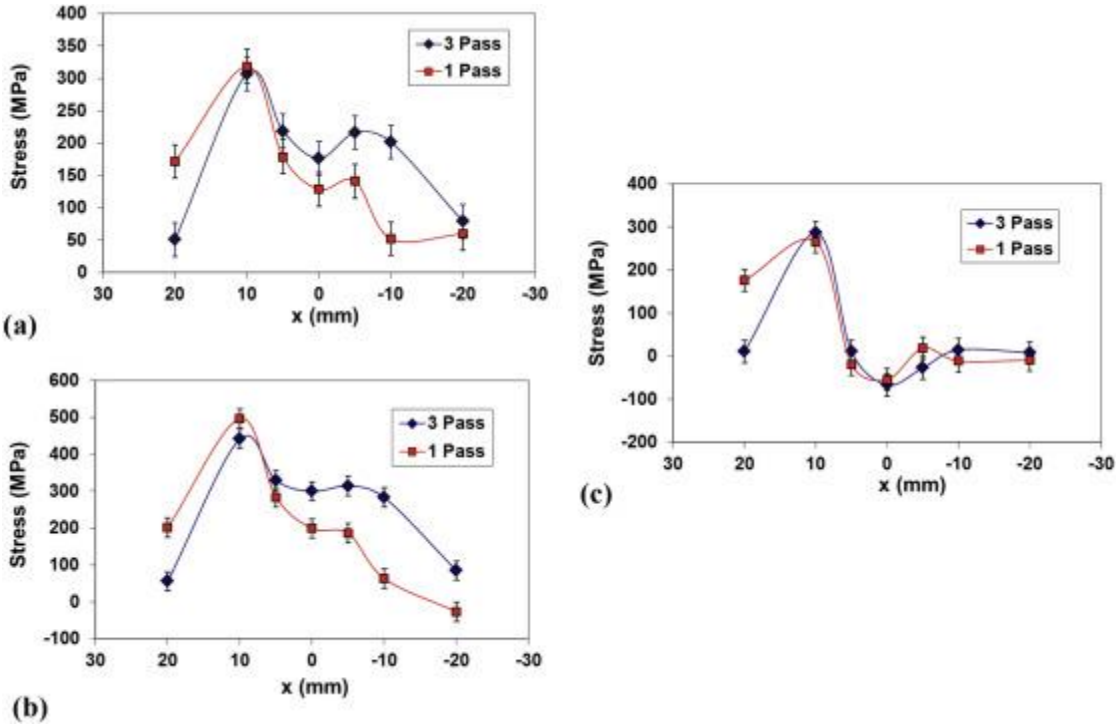


Fig. 10.

Comparison of the results of '*map*' measurements on the single-pass and triple-pass weldments, at α = 0, r = 137.5 mm for (a) Axial (b) Hoop (c) Radial stress component.

The axial stress component peaks near x = +10, with increasing tensile stress as the HAZ is approached in both weldments, with a wider spread of stress in the triple-pass weldment. The hoop stress component also peaks near x = +10 and is tensile at all values of x. There is a wider spread of stress in the triple-pass weldment. The radial stress component exhibits a similar trend, but is more similar for both weldments. At other angles *α* where measurements were made these effects are not so evident and there is a general decrease in stress levels.

**5. Finite element measurements**

Three-dimensional Finite Element analyses of both the single and triple-pass weldments were carried out using the Quick Welder FEM code [8]. The relatively simple mesh used for these simulations is shown in Fig. 11 and comprised 17,568 nodes and 21,030 elements. The mesh in the hoop direction was divided into 72 elements.

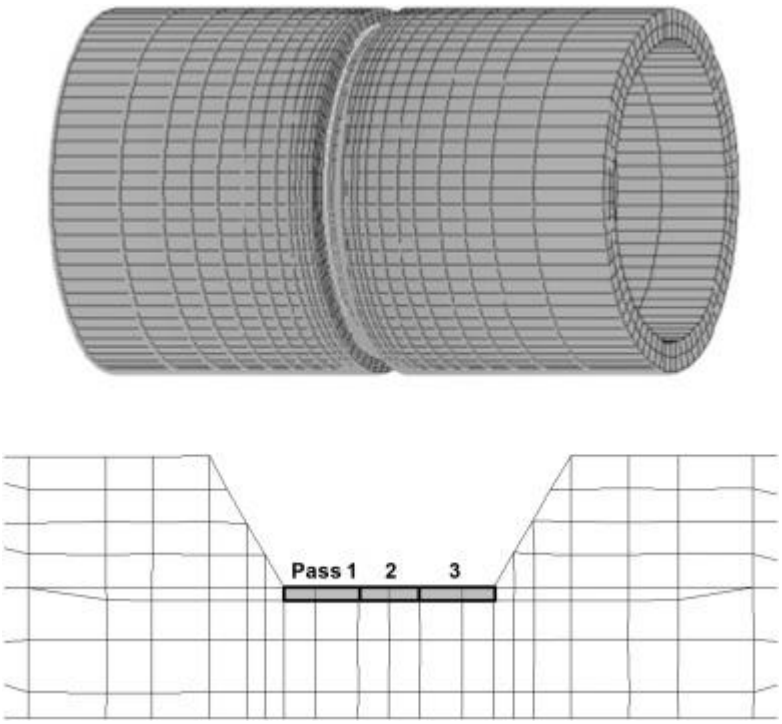


Fig. 11.

FEM mesh for non-filler welded pipe.

The temperature-dependent properties were as shown in Table 2[9], with density 7900 kg/m$^3$.

Table 2.

Thermal properties of material as a function of temperature [9]. A bi-linear idealization of the stress-strain curve relates the yield stress, ($S_Y$) and the hardening modulus, (H').

| **Temp./ °C** | **Specific heat/kJ/(kgK)** | **Conductivity/W/(mK)** | **Thermal expansion/$10^{-6}$ °C$^{-1}$** | **Young's modulus/GPa** | **Poisson's ratio** | **Sy/MPa** | **H'/MPa** |
|---|---|---|---|---|---|---|---|
| 20 | – | – | – | – | – | 229 | 1772 |
| 25 | 0.462 | 14.6 | 15.4 (30 °C) | 198.5 | 0.294 | | |
| 100 | 0.496 | 16.1 | 15.9 | 192.8 | 0.295 | | |
| 200 | 0.512 | 17.6 | 16.4 | 184.7 | 0.301 | 139 | 1912 |
| 300 | 0.525 | 18.9 | 17.2 | 175.9 | 0.310 | – | – |
| 400 | 0.540 | 20.3 | 17.7 | 167.3 | 0.318 | 115 | 1796 |
| 500 | 0.559 | 22.1 | 18.2 | 159.0 | 0.326 | – | – |
| 600 | 0.577 | 23.8 | 18.4 | 150.8 | 0.333 | 106 | 1802 |
| 700 | 0.592 | 25.5 | 18.7 | 142.6 | 0.339 | – | – |
| 800 | 0.604 | 26.9 | 19.0 | 133.6 | 0.342 | 87 | 110 |
| 900 | – | – | 19.2 | 115.8 | 0.388 | – | – |
| 1000 | 0.644 | 30.7 | 19.5 | 95.4 | 0.370 | 26 | 69 |
| 1100 | – | – | 19.7 | – | – | – | – |
| 1200 | 0.676 | 35.2 | 20.0 | – | – | – | – |
| 1300 | 0.692 | 36.7 | 20.3 | – | – | – | – |

A bi-linear isotropic hardening constitutive model was applied in these analyses with an annealing temperature of 800 °C. Volumetric heat input was applied to each of the gray elements shown in Fig. 11. The heat input to the elements at the weld stop and start positions was the same as for the other elements. The welding current, voltage, speed and efficiency were 130 A, 10 V, 90 cm/min and 0.75, respectively.

The FEM results for the axial and hoop stress components at $r$ = 137.5 are compared with the corresponding neutron measurements in Fig. 12. The simulated and measured stress components are in agreement for the axial stress component, and the transition from tensile to compressive stress at $\alpha$ = 0 can be clearly seen. The agreement for the hoop stress component is reasonably good for the multi-pass weld but is not so good for the single pass weld, where, although the trends and

tensile nature of the stress are evident, the neutron measurements reveal less tensile stress than that FEM calculations.

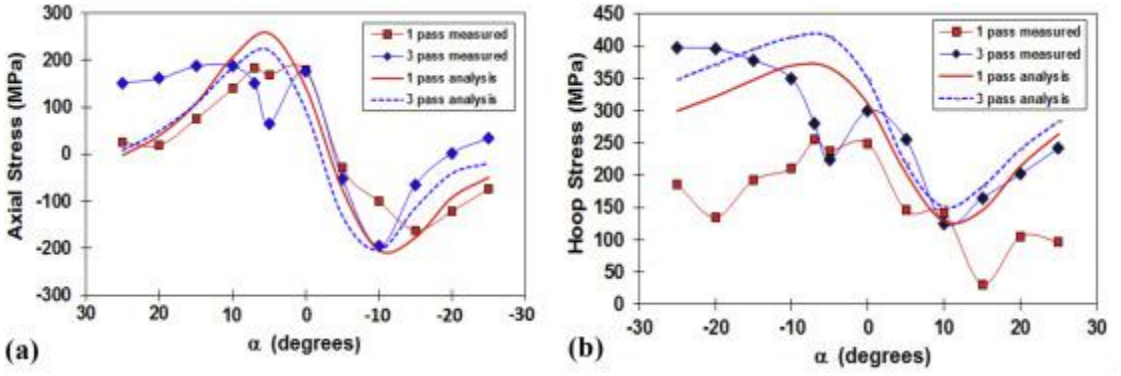


Fig. 12.

Comparison of the FEM assessment of (a) Axial (b) Hoop residual stress components with the neutron diffraction results for 'arc' measurements at x = 0, r = 137.5 mm. The FEM results are the continuous and broken lines for the one-pass and triple-pass weldments, and the neutron results the diamond and square points respectively.

In this work heat was applied to the pipes alone, without filler, and it is considered that the measured and simulated results, using the relatively simple model, are in reasonable overall agreement.

**6. X-ray measurements of the near inner surface residual stress components**

A specially-adapted X-ray diffractometer was used to make measurements of stress near the inner surface under the welds. X-rays from a manganese target were diffracted at a scattering angle of ~152° into two detectors, with a 4° oscillation. A 3 mm slit defined the beam. The surface at the positions of measurement was electrochemically polished to obtain a depth profile to 200 µm. Measurements were made of the axial and angular variation of the hoop stress component of residual stress in both weldments. Some of the results of these inner surface measurements of the hoop stress component are shown in Fig. 13. Fig. 13(a) shows that the axial variation of the hoop stress component peaks at the centre of the weldment at x = 0.0, with the single-pass weldment exhibiting the higher tensile residual stress. The angular variation of the hoop stress component shown in Fig. 13(b) and (c) for the single-and triple-pass weldment respectively shows a tensile stress with little variation between the two axial positions in both weldments.

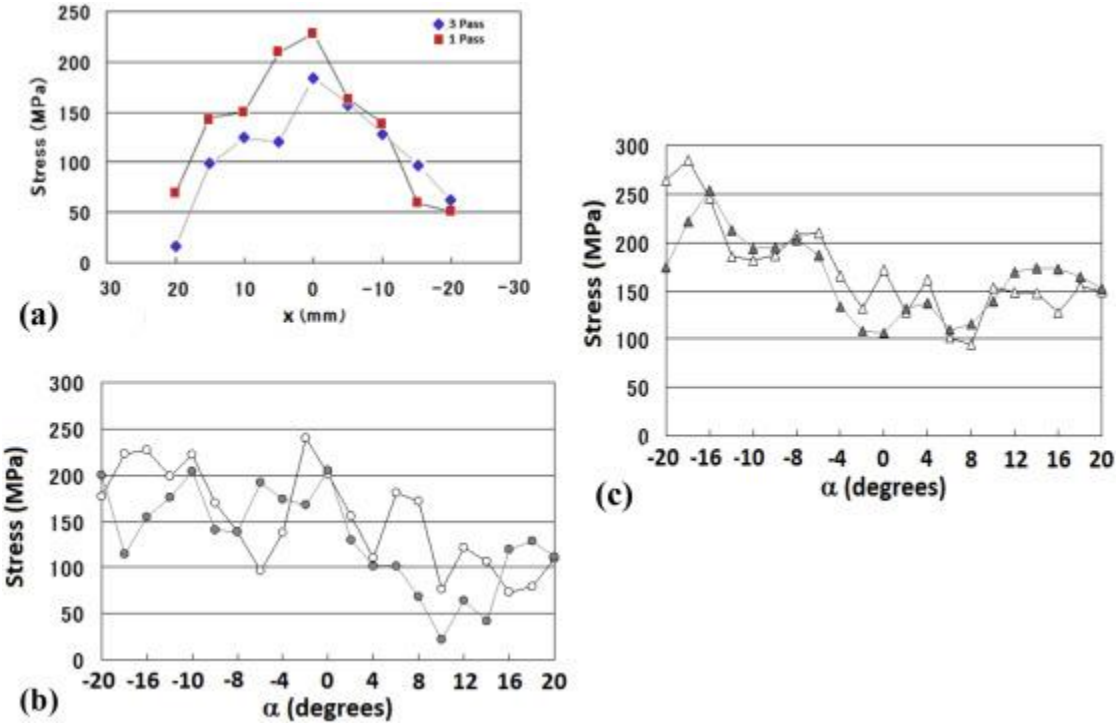


Fig. 13.

X-ray diffraction measurements. (a) The axial variation of the hoop component of residual stress, measured on the inner surface of the single-pass and triple-pass weldment. (b) The angular variation of the hoop component of residual stress measured on the inner surface of the single-pass weldment, open circles under centre of groove at x = 0.0, and closed circles under first pass at x = +6.6 mm. (c) The angular variation of the hoop component of residual stress measured on the inner surface of the triple-pass weldment, open triangles under centre of groove at x = 0.0, and closed triangles under first pass at x = +6.6 mm.

**7. Conclusions**

1.

Neutron diffraction measurements have been made of the variation of the residual stress components in a single-pass and a triple-pass weldment of austenitic stainless steel type 304. Results have been compared with stress assessments made using the Finite Element technique, and X-ray diffraction measurements of the near surface stress hoop component on the inside of the weldments. The residual stress variation was determined with position along the axis through the weld groove, at three radii through the thickness, and at a number of azimuthal angles around the weld.

2.

Although there is considerable scatter in the neutron diffraction results owing to experimental uncertainties, key features of the residual stress profiles can be determined. In the variation of stress with azimuthal angle α, at the centre of the groove x = 0 the axial stress component undergoes a marked transition from tension to compression through α = 0. The variation in the tensile hoop stress component is from higher tensile to lower tensile stress. This effect is larger in the single-pass than in the triple-pass weldment. The radial stress component is close to zero stress, and shows little variation with α.

3.

The hoop stress component is found to be generally tensile, and greater in the triple-pass weldment than in the single pass weldment. The hoop stresses reach peak values of around 400 MPa in tension.

4.

Finite element analysis is in good agreement in the comparison of the axial stress component, but the hoop stress component differs in magnitude of the tensile stress. X-ray measurements from the inner near surface stress hoop component show tensile stresses in both pipes, with a higher magnitude in the three-pass weldment.

**Acknowledgements**

The authors are grateful to JNES for the funding of this work. The neutron beam time was provided by the Institut Laue-Langevin. MEF is grateful for funding from the Lloyd's Register Foundation, a charitable foundation helping to protect life and property by supporting engineering-related education, public engagement and the application of research. The authors are also grateful to Dr Olivier Zanellato for help with this experiment and to Professor John Bouchard for useful discussions.

**References**

[1] P.J. Bouchard. Int J Press Vessel Pip, 84 (2007), pp. 195–222

[2] P.J. Bouchard. Int J Press Vessel Pip, 85 (2008), pp. 152–165

[3] L. Edwards, M.C. Smith, M. Turski, M.E. Fitzpatrick, P.J. Bouchard. Adv Mater Res, 41–42 (2008), pp. 391–400

[4] P.J. Withers, M. Turski, L. Edwards, P.J. Bouchard, D.J. Buttle. Int J Press Vessel Pip, 85 (2008), pp. 118–127

[5] M.T. Hutchings, P.J. Withers, T.M. Holden, T. Lorentzen. Introduction to the chracterisation of residual styresses by neutron diffraction. CRC Press, Taylor & Francis (2005)

[6] R.D. Haigh, M.T. Hutchings, J.A. James, S. Ganguly, R. Mizuno, K. Ogawa, et al. Int J Press Vessel Pip, 101 (2013), pp. 1–11

[7] T. Pirling, G. Bruno, P.J. Withers. Mater Sci Eng A, 437 (2006), pp. 139–144

[8] S. Kiyoshima. Quick welder user's manual. Research Center of Computational Mechanics Inc. (2005)

[9] Project of integrity assessment of flawed components with structural discontinuity (IAF) material properties data book at high temperature for dissimilar metal welding in reactor pressure vessel, JNES-RE-2012-0024 (2012)

[10] M.C. Smith, A.C. Smith, R. Wimpory, C. Ohms. Int J Press Vessel Pip, 120–121 (2014), p. 93

[11] D.J. Smith, G. Zheng, P.R. Hurrell, C.M. Gill, B.M.E. Pellereau, K. Ayres, et al. Int J Press Vessel Pip, 120–121 (2014), p. 66

[12] P.J. Bouchard. Int J Press Vessel Pip, 86 (2009), p. 31

[13] A. Skouras, P.E.J. Flewitt, M. Peel, M.J. Pavier. Int J Press Vessel Pip, 123–124 (2014), p. 10

[14] A. Elmesalamy, J.A. Francis, L. Li. Int J Press Vessel Pip, 113 (2014), p. 49

[15] W. Woo, G.B. An, E.J. Kingston, A.T. DeWald, D.J. Smith, M.R. Hill. Acta Mater, 61 (2013), p. 3564

[16] A. Skouras, A. Paradowska, M.J. Peel, P.E.J. Flewitt, M.J. Pavier. Int J Press Vessel Pip, 101 (2013), p. 143

[17] O. Muransky, T.M. Holden, O. Kirstein, J.A. James, A.M. Paradowska, L. Edwards. J Nucl Mater, 438 (2013), p. 154

[18] A. Kundu, P.J. Bouchard, S. Kumar, K. Venkata, J. Francis, A. Paradowska, et al.. Sci Technol Weld Join, 18 (2013), p. 70

[19] S. Paddea, J.A. Francis, A.M. Paradowska, P.J. Bouchard, I.A. Shibli. Mater Sci Eng A, 534 (2012), p. 663

[20] A.S. Aloraier, S. Joshi. Mater Sci Eng A, 534 (2012), p. 13